Temperature and pressure effects on the electrochemical CO2 reduction

Vos, R.E.

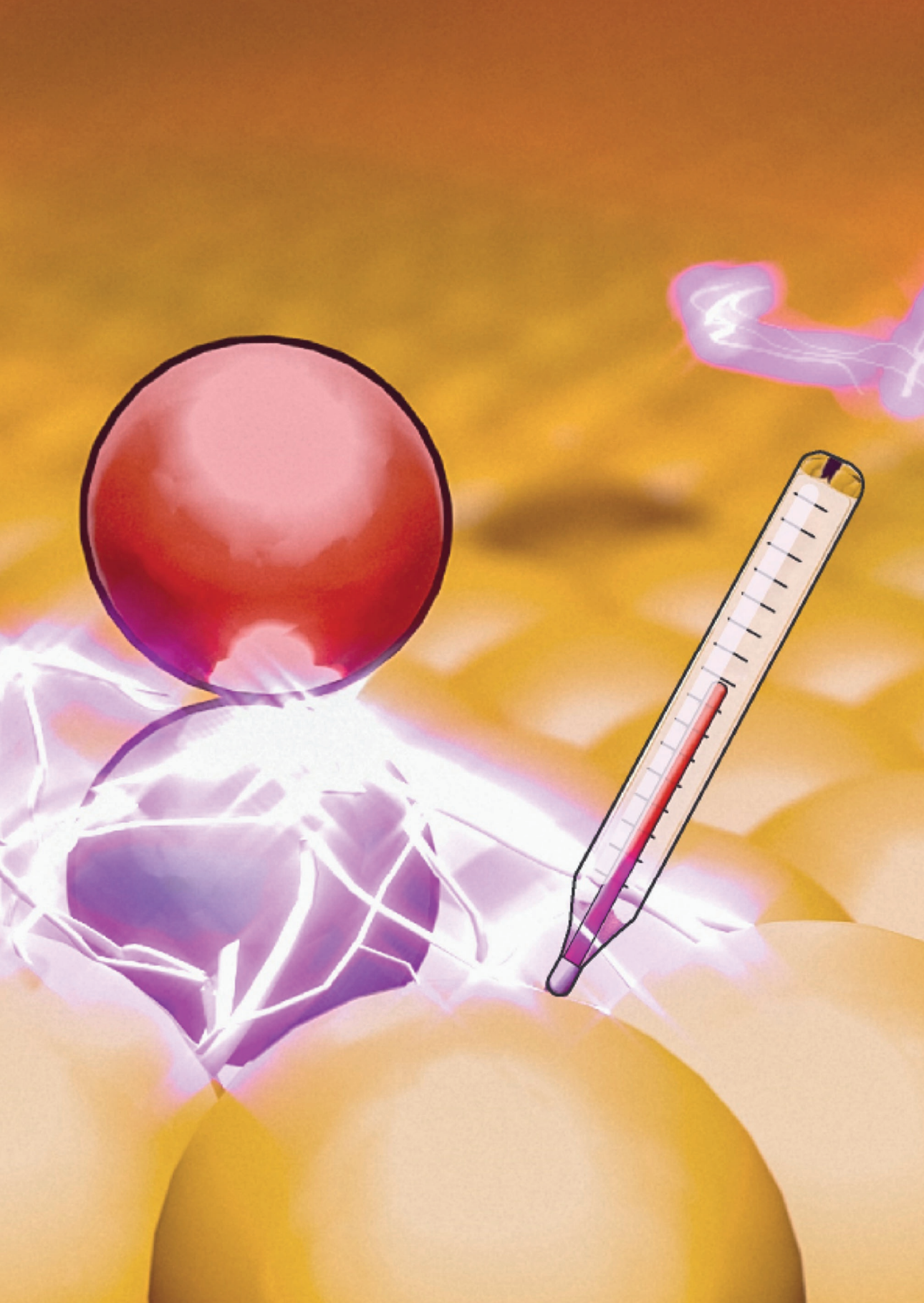

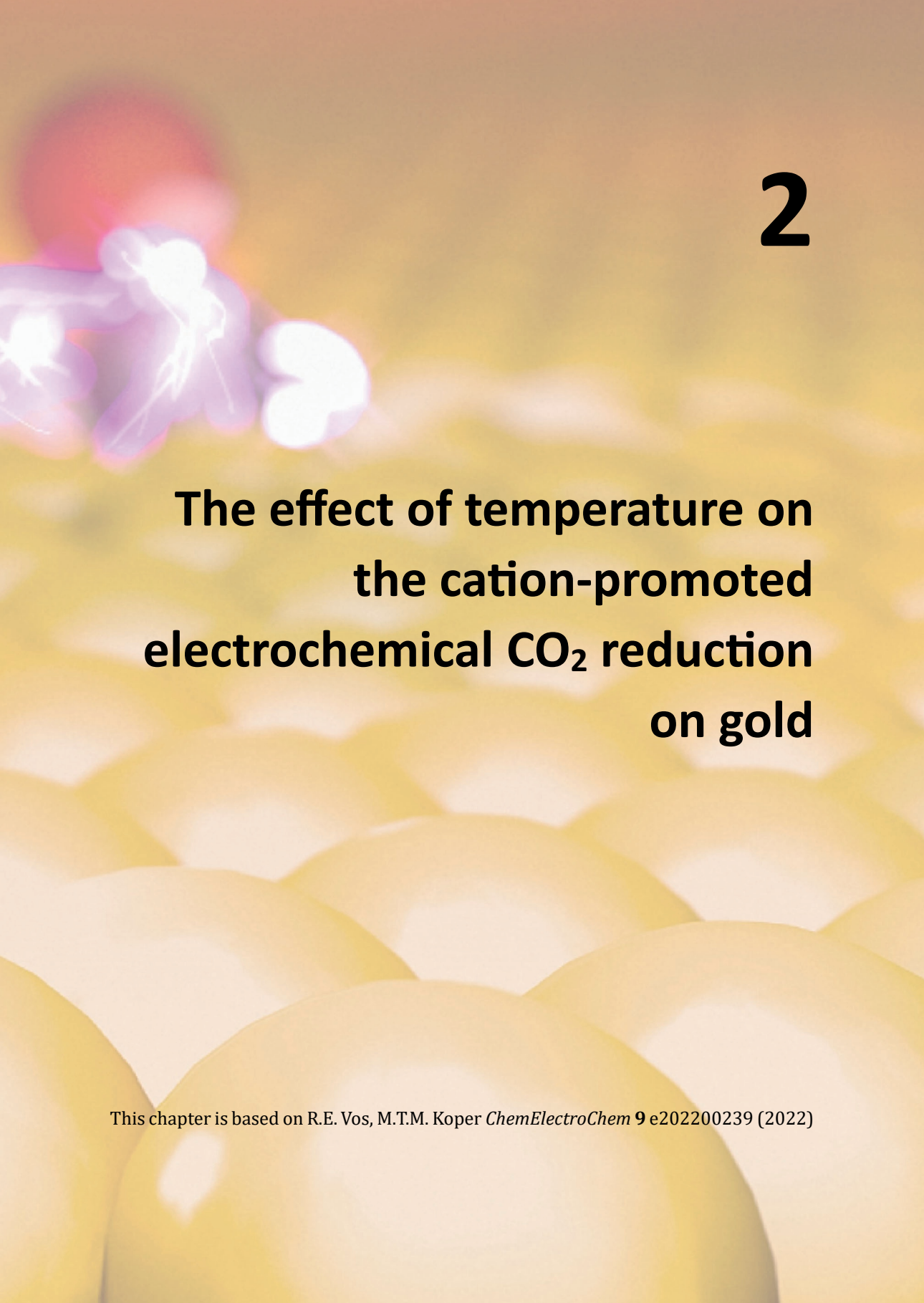

2

The effect of temperature on the cation-promoted electrochemical CO_2 reduction on gold

This chapter is based on R.E. Vos, M.T.M. Koper *ChemElectroChem* **9** e202200239 (2022)

Abstract:

Electrochemical reactions in general, and the CO_2 reduction reaction (CO2RR) in particular, are commonly studied at room temperature. However, practical electrolysers may use elevated temperatures. There is currently a lack of fundamental understanding of the effect of temperature on the CO2RR. Here, we have performed temperature-dependent studies on the CO2RR on a relatively simple electrode material, namely gold, to obtain insights into how temperature influences this reaction and the competing hydrogen evolution reaction. A rotating ring disk electrode setup has been used to show that the CO2RR activity and selectivity increases with temperature, and to obtain kinetic parameters such as the apparent activation energy and transfer coefficient. The magnitude of the temperature effect and the activation energy is affected by both the cation identity and concentration in the electrolyte. Moreover, the positive effect of temperature on the kinetics of the CO2RR is counteracted by the lower CO_2 solubility, making efficient mass transport even more important at higher temperatures.

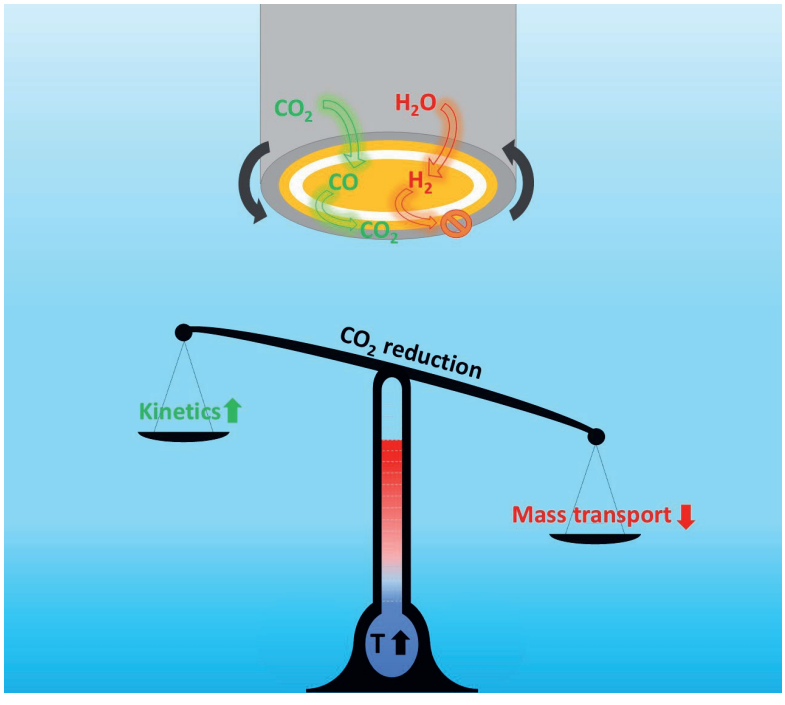

2.1 Introduction

Electrochemical CO_2 reduction (CO2RR) has the potential to generate clean fuels and building blocks for the chemical industry with CO_2, water and renewable energy, thereby creating a closed carbon cycle without the use of fossil fuels. This reaction has gained substantial attention and many aspects of CO_2 reduction have been studied,[1,2] such as catalyst material and the effect of the electrolyte. Electrolyte properties ranging from pH,[3–7] buffer capacity,[8–10] cations,[11–14] and anions,[15,16] to catalyst properties such as the facet,[17–20] defects,[21,22] morphology[23–25] and roughness, [4,26,27] have all been shown to influence the activity and selectivity for the CO2RR and the competing hydrogen evolution reaction (HER).

An aspect which has been studied less is the effect of temperature on CO_2 reduction. Most electrochemical experiments have been performed at room temperature and ambient pressure, even though most industrial (water) electrolyzers work at slightly elevated temperatures.[28–32] Some degree of heating is intrinsic to these industrial systems as they are the consequence of overpotentials and resistive losses.[32,33] Moreover, the sources of concentrated CO_2, for example from electricity production or steel manufacturing, often emit hot CO_2. The temperature during the electrochemical CO2RR could also be deliberately increased to increase activity and selectivity or to open up new mechanisms and generate other products.

Although some studies do include a section with temperature dependent experiments,[34–37] there are not many systematic studies on the effect of temperature on the CO2RR.[1,38] Systematic studies are important to elucidate how temperature exactly influences the reaction, as various aspects of the system may change with changing temperature. One of the most important changes is the solubility of CO_2, which decreases with increasing temperature. This results in a change in pH, which will also change due to the difference in acid-base equilibria such as the water disproportionation at different temperatures. Furthermore, reaction rates, diffusion coefficients, equilibrium potentials, and the conductivity of solution and membranes all change with temperature.

One of the few systematic studies on the effect of temperature on CO_2 reduction has been done by Ahn et al.[39] They studied a Cu electrode at -1.60 V vs Ag/AgCl at temperatures from 2 to 42 ^{0}C in a 0.1M $KHCO_3$ electrolyte. They showed that methane is the dominant product at low temperatures, but the faradaic efficiency (FE) decreases with increasing temperature. For ethylene, there seems to be an optimum in the FE at medium temperatures. At the highest temperature, 42 ^{0}C in the mentioned study, the system is dominated by the parasitic hydrogen evolution.

They attributed these observations to the combined effect of CO_2 solubility and local pH. These results are mostly in agreement with experiments by Hori et al., [40] although they did not see an optimum in ethylene production in this temperature range.

Most studies on the effect of temperature on the CO2RR are not performed in a H-cell, but in a GDE (Gas Diffusion Electrode) setup. Dufek et al.[31] studied an Ag GDE at 18, 35 and 70 ^{0}C in a 0.5 M K_2SO_4 electrolyte. They observed a decrease in both cell and cathodic potential with increasing temperature. This decrease is not surprising as the conductivity of both the electrolyte and the membrane will increase with increasing temperature, lowering the ohmic drop. Moreover, they observed that the FE for CO increases at higher current densities when the temperature goes from 18 to 35 ^{0}C, but decreases again at 70 ^{0}C. In terms of activity, a plateau is observed for CO formation. The activity first increases from 18 to 35 ^{0}C and remains the same for 35 and 70 ^{0}C. This plateau was associated with mass transport limitations of CO_2.

Löwe et al.[41] used a Sn GDE and observed a decrease in the required potential at higher temperatures, similar to Dufek et al. [31] This resulted in a small shift in product distribution from HCOOH to CO. When CO_2 becomes mass transport limited, they noticed an increase in HER. With increasing the temperature from 25 ^{0}C to 50 ^{0}C, they observed an increase in the potential at which this happens, but a further increase of the temperature to 70 ^{0}C resulted in the reverse trend. This optimum was attributed to the interplay of the diffusion rate which increases with temperature and the CO_2 solubility which decreases with temperature. In summary, all mentioned studies observed effects at elevated temperatures which are assumed to be an indirect effect of temperature on the mass transport limitation. The intrinsic effect of temperature on the CO_2 reduction reaction rate is concealed by these indirect effects.

An aspect of CO_2 reduction that has recently been studied in some detail is the cation effect. It has been shown that the activity of the CO2RR is significantly influenced by the nature of the cation. An activity trend $Cs^+ > K^+ > Na^+ > Li^+$ has been observed at several electrode materials,[12,42–44] whereas on Cu the

selectivity towards C2+ products also increases in this order.[12,13] There are three main theories proposed to explain this cation effect.[45] Some studies attribute the cation effect to differences in the local pH,[13,46,47] where Cs^+ buffers better than Li^+. Other explanations focus on the effect of the electric field, which changes with the size of the cation. This electric field then either stabilizes intermediates [12,14,48] or changes the local potential in the outer Helmholtz layer.[11] Besides the electric field,

also short-range electrostatic interactions can help stabilize the intermediates. [48] However, the cation effect has not been studied yet in combination with varying temperature.

In this study, we systematically studied the effect of temperature on CO_2 reduction. We used Au as a catalyst to simplify the system as only CO and H_2 are produced in significant amounts.[49–51] We performed partial pressure experiments to study the effect of temperature and CO_2 solubility independently. A rotating ring disk electrode (RRDE) setup was used to deconvolute the current to the CO2RR and the HER,[52] and to control and improve mass transport. With a diffusion layer thickness in the range of 1µm,[53] the RRDE allows for a better study of the intrinsic catalytic activity of the electrochemical reduction processes. We show that both activity and selectivity of CO_2 reduction are increased with temperature, although there is a complex balance between the effect of increased kinetics and decreasing CO_2 concentration. Furthermore, we extract kinetic data such as the transfer coefficient and the apparent activation energy. We show that the latter is influenced by the cation and that therefore the magnitude of the temperature effect depends on the electrolyte used.

2.2 Experimental Section

2.2.1 Chemicals

The electrolytes were prepared from H_2SO_4 (98%, EMSURE, Merck), $NaHCO_3$ (≥99.7%, Sigma Aldrich), Li_2CO_3 (99.997%, Sigma Aldrich), $KHCO_3$ (99.95%, Sigma Aldrich), $CsHCO_3$ (99.99%, Alfa Aesar), $NaClO_4$ *H_2O (Emsure, Merck) and Milli-Q water (≥18.2 MΩcm, TOC < 5 ppb). Ar (6.0 purity, Linde), CO_2 (4.5 purity, Linde), and H_2 (5.0 purity, Linde) were used for purging the electrolytes. For the dopamine modification, the RRDE tip was coated using dopamine hydrochloride (≥98.5%, Sigma-Aldrich). To determine the collection efficiency, $K_3Fe(CN)_6$ (>99%, Sigma-Aldrich) was used.

2.2.2 General Electrochemical Methods

All experiments were performed using homemade borosilicate glass cells, which were cleaned prior to experiments by storing the cells in an acidified (0.5 M H_2SO_4) $KMnO_4$ solution (1 g/L) overnight. Before experiments, the glassware was submerged in diluted piranha to remove any traces of MnO_4 and MnO_2. Then the cells were boiled at least three times with MilliQ water. Experiments were performed in a three-electrode configuration where the reference electrode was separated from the working compartment with a Luggin capillary. The reference electrode was either a home-made RHE or, for the temperature-dependent

measurements, a commercial RHE from Gaskatel, which was placed in the cell to be at the same temperature as the working electrode. The counter electrode was a gold wire (99.99% purity). The working electrode was a gold disk in a PEEK shroud with gold ring (E6/E5 ChangeDisk tips, Pine research) and the RRDE measurements were performed with a Modular Speed Rotator (Pine research). All the electrochemical measurements were carried out using an IviumStat bipotentiostat (Ivium Technologies). For the activity measurements, 85% ohmic drop compensation was performed. The ohmic drop was determined by electrochemical impedance spectroscopy (EIS) at 0.05 V vs RHE. Before experiments, the electrolytes were purged with either Ar or CO_2 for at least 15 minutes and purging continued during measurements. To control the temperature a water bath was used (Ecoline e100, Lauda). For the partial pressure experiments, the flow of CO_2 and Ar was set accordingly using two mass flow controllers (SLA5850, Brooks Instrument).

2.2.3 Working Electrode Preparation and Dopamine Modification

The RRDE method used in this study has been developed in our group and described in detail in a previous publication.[52] In this study, we slightly modified some steps. Before each experiment, the gold disk (diameter = 5 mm, Pine Instruments) was mounted in the RRDE tip which contained a gold ring. The tip was mechanically polished with decreasing diamond polishing suspension (3.0, 1.0 and 0.25 μm) on Buehler micropolishing cloths (8 in.). After polishing, the tip was successively sonicated in ethanol and water for 3 min to remove any impurities. Next, the Au disk and ring were short-circuited and electrochemically polished in 0.1 M H_2SO_4 by cycling into the Au oxide formation and reduction region (0.05 – 1.7 V vs RHE, 200 cycles at 1 V/s). A characterization cyclic voltammogram (CV) of the ring and disk was obtained in this same potential window at a scan rate of 50 mV/s. Next, the RRDE tip was modified by coating with dopamine to prevent bubble attachment on the Teflon spacer between the disk and the ring of the RRDE tip.[54] This bubble attachment leads to noise in the CO oxidation current on the ring. The dopamine modification was performed by immersing the RRDE tip in a 2 g/L solution of dopamine hydrochloride (prepared with 20 mL of bicarbonate electrolyte). This was done for 1 hour at about 55 ^{0}C, while the RRDE was rotated at 450 rotations per minute (rpm). After the coating, any dopamine on the ring and the disk had to be removed. This was done by electrochemical polishing in 0.1M H_2SO_4 once again for 200 cycles. Next, 75 cycles were performed in the same potential range but in the measurement cell with CO_2 saturated bicarbonate solution. This was followed by a reduction going to -1.0 V vs RHE at 50 mV/s for 3 cycles in the measurement cell and a polishing step in H_2SO_4 for 100 cycles. Then, a characterization CV was obtained for the ring and disk, which was compared with the CV of the unmodified surface. A good agreement between these CVs indicated

that the surface morphology had not changed significantly during the coating procedure and that any dopamine was removed from the ring and disk.

2.2.4 RRDE CO_2 reduction measurements

After the working electrode was prepared as described above, the CO2RR measurements were performed in the measurement cell with a CO_2 saturated 0.1 M bicarbonate electrolyte. This measurement cell was placed in a water bath to control the temperature in the cell. For the measurements, the disk was cycled from 0.05 to -1.0 V vs RHE in a bicarbonate electrolyte with a scan rate of 20 mV/s. The ring current was measured simultaneously, while the ring potential was set to 1.0 V vs RHE. The measurements were performed with two different rotation speeds, namely 1200 and 2500 rpm. At each temperature, both rotation rates were measured three times in an alternating way. These three measurements were averaged afterwards. In order to make sure that the surface did not change during measurements, the disk and ring were short-circuited after every individual measurement and cycled 8 times in the Au oxide formation/reduction potential window (0.05 – 1.75 V vs RHE at 1 V/s) in the measurement cell.

Between every set of measurements at a given temperature, the RRDE tip was electrochemically polished in 0.1 M H_2SO_4 and a characterization CV was obtained for the disk. The electrochemically active surface area (ECSA) of the disk was determined by calculating the charge of the reduction peak in this characterization CV and dividing this by the specific charge of one monolayer of Au (390 μC/cm^2).[55] Then, the tip was transferred to the measurement cell and cycled from 0.05 – 1.75 V vs RHE at 1 V/s for 75 cycles to stabilize the temperature of the cell and the tip. Thereafter, the resistance was determined using electrochemical impedance spectroscopy (EIS) and compensated for 85% in the measurement CVs. Next, the measurements could start as described above.

2.2.5 Collection Efficiency Determination

The apparent collection efficiency of the ring was determined at the end of a day of experiments to account for the changes in tip geometry that incur with the assembling of the tip. The apparent collection efficiency was determined in a separate cell containing 0.1 M Ar saturated $NaHCO_3$ with 5 mM $K_3Fe(CN)_6$. The disk was cycled between 0.27 and 1.27 V vs RHE and the ring potential was set to 0.96 V vs RHE. The collection efficiency was determined for each rotation rate and was calculated according to equation 2.1:

$$N = \left|\frac{i_{ring}}{i_{disk}}\right| \qquad (2.1)$$

2.2.6 The CO2RR and HER Current Deconvolution

The selective oxidation of CO on the gold ring, under diffusion limited conditions, makes it possible to deconvolute the CO2RR and the HER current under the assumption that H_2 and CO are the only products on the Au polycrystalline disk in the potential window used in this study. This assumption is reasonable as studies have determined CO as the only appreciable product of CO2RR on gold.[49–51] The partial current density for CO formation can be calculated from the experimental ring current (i_{ring}) and the apparent collection efficiency N:

$$J_{CO} = \frac{-i_{ring}}{N * ECSA_{disk}} \qquad (2.2)$$

The Faradaic efficiency for CO formation can be calculated as

$$FE_{CO} = \frac{i_{ring}}{|i_{disk}| * N} * 100\% \qquad (2.3)$$

The partial current density and faradaic efficiency for the HER can be calculated from

$$J_{H_2} = J_{tot} - J_{CO} \qquad (2.4a)$$

$$FE_{H_2} = 100 - FE_{CO} \qquad (2.4b)$$

2.2.7 Temperature dependence of the reference electrode

It is important to choose a proper reference electrode to conduct temperature dependent electrochemical experiments. The reference potential depends explicitly on the temperature via the entropy term, but also implicitly via the standard potential and the activity of ions. Specifically, for the Ag/AgCl and the RHE electrode:

$$E^{Ag|AgCl} = E^{0,\,Ag|Ag^+} + \frac{RT}{F}\ln(K_s) - \frac{RT}{F}\ln(a_{Cl^-}) \qquad (2.5a)$$

$$E^{RHE} = E^{SHE} - \frac{RT\lambda}{F}\mathrm{pH} \qquad (2.5b)$$

In many high-temperature corrosion studies, Ag/AgCl has been used as reference electrode.[56] To determine the potential of the Ag/AgCl electrode, empirical formulas have been used both to correct for the temperature dependence of the standard potential, the solubility product, and the activity of chloride ions.[57–59] However, it would be easier if one could employ a RHE reference. The SHE is namely defined zero at all temperatures and the only implicit temperature

dependent term left is the pH, which can be measured experimentally. Furthermore, it is important that the reference electrode is at the same temperature as the working electrode, otherwise other unknown potential drops can occur due to the temperature gradient.[56] This is why we have chosen to work with an RHE reference from Hydroflex, as this can easily be kept at the same temperature as the working electrode and no extra correction is needed as with an Ag/AgCl electrode.

2.2.8 Determination of apparent activation energy

The exchange current density was used to calculate the apparent activation energy. The exchange current density of CO formation was determined from a Tafel plot (Figure A.1). The current density between -0.575 and -0.775 V vs RHE was extrapolated to the standard equilibrium potential of CO_2 reduction towards CO. This potential range was chosen due to practical considerations: between -0.3 and -0.4 V the currents are too low for an accurate extrapolation, whereas between -0.4 and -0.5 the Tafel plot is too strongly curved for a reliable extrapolation (see Figure A.1). The standard equilibrium potential was calculated for each individual temperature (Table A.2).

2.3 Results and Discussion

2.3.1 Temperature effect on activity and selectivity of the CO2RR and HER

Figure 2.1 shows the effect of temperature on the activity of CO_2 reduction and hydrogen evolution on a gold electrode at 2500 rpm. The partial current density for CO increases with increasing temperature up to 50-55 ^{0}C. For T > 50-55 ^{0}C, there is a plateau in the activity of the CO2RR, which can more clearly be seen in Figure A.2. No qualitative differences are observed when the SHE scale (Figure A.3) is used instead of the RHE scale. With increasing temperature, several aspects of this system change which can cause this behavior (see Figure A.4). The CO_2 solubility decreases with temperature,[60–62] while the diffusion coefficients increase. [63–65] Reaction equilibria shift with temperature and reaction rate constants will increase increasing temperature.[66] The thermodynamic equilibrium potential also shifts with temperature, meaning that the same absolute potential does not give the same overpotential. However, calculations show this shift is less than 16 mV in the temperature range studied (Table A.2) and that it shifts negatively with increasing temperature, so most of the changes in activity will be governed by kinetics and diffusion and not the thermodynamics of the CO2RR. The conductivity of the electrolyte increases with temperature, at least for aqueous electrolytes up to 90 ^{0}C.[66] Although this is not relevant for this study as we perform IR correction, it can

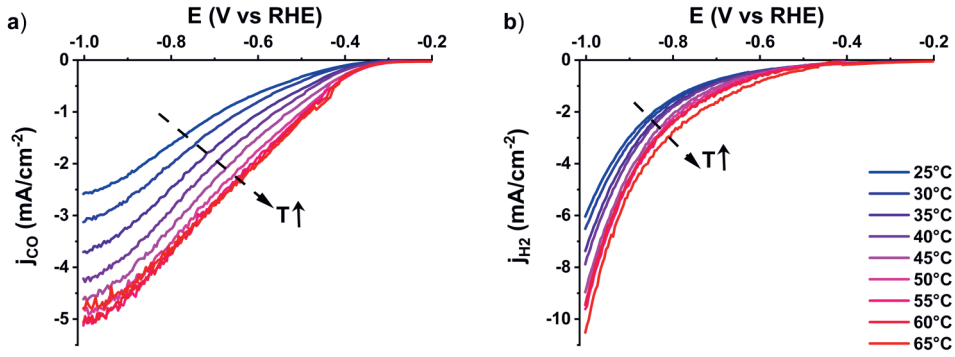

Figure 2.1 The partial current density towards CO formation (a) and H_2 (b) at different temperatures in 0.1M $NaHCO_3$ on a gold RRDE at 2500 rpm and 20 mV/s

be an important consideration for practical applications of electrolyzers, as this will decrease the cell potential and could increase the cell efficiency. [32]

In general, the pH tends to decrease with temperature due to increased ionization of water.[66] However, in our system, the CO_2 concentration decreases with temperature and due to the complex equilibria with bicarbonate, carbonate, hydroxide and water, the net change in pH is an increase of about half a pH unit from 25 to 70 ^{0}C (Figure A.4). Moreover, the buffer capacity decreases as both the CO_2 and HCO_3^- concentrations decrease with temperature.[67] This means that the local pH can increase even more with temperature than the bulk pH, also because the currents increase with temperature. As we are using the rotating disc electrode, minor differences between the bulk and local pH could be expected. Zhang et al.[46] have shown that for low current densities (<4.33 mA/cm^2 at 1600 rpm) no significant local pH changes are observed. On the other hand, recent experiments in our group have shown that even at relatively low current densities, the local pH at rotating electrodes can be significantly different from the bulk pH.[68] However, as the change in bulk pH and buffer capacity are minor, we do not expect the pH to dominate the temperature effect observed in Figure 2.1. The local pH can change because the current densities are higher, but this is then the result of the increased activity, instead of the cause. Moreover, the local pH tends to influence the FE by influencing the activity of the HER rather than the activity of the CO2RR.[69,70]

The solubility of CO_2 is an important factor which depends on the temperature according to the van 't Hoff equation. The solubility can be estimated with Henry's law:

$$C = KP \qquad (2.6)$$

where C is the concentration, K is the Henry's constant and P is the partial pressure. The Henry's constant depends on temperature and we used the empirical equation 2.7 to calculate this dependence.[62]

$$\log(K) = 108.3865 + 0.01985076 * T - \frac{6919.53}{T} - 40.4515 * \log(T) + \frac{669365}{T^2} \qquad (2.7)$$

With the use of Henry's law, we can deconvolute the effect of CO_2 concentration from the overall effect of temperature. By changing the partial pressure at constant temperature, the effect of CO2 concentration can be studied independently of the effect of temperature. It is expected that if the concentration of CO_2 in the bulk is altered, a corresponding change in the CO_2 concentration at the surface of the electrode will occur.[67] Figure A.5 shows that the activity for the CO2RR decreases with decreasing dissolved CO_2 concentration. This trend is as expected and has been observed in literature before.[71–73] The corresponding reaction order of CO_2 is 0.9 (Figure A.6), which is comparable with literature.[73–75]

We have studied the effect of temperature independent of the CO_2 concentration by adjusting the partial pressure at different temperatures. As the "standard" concentration we take the CO_2 concentration at 1 atm of CO_2 at 70 ^{0}C.

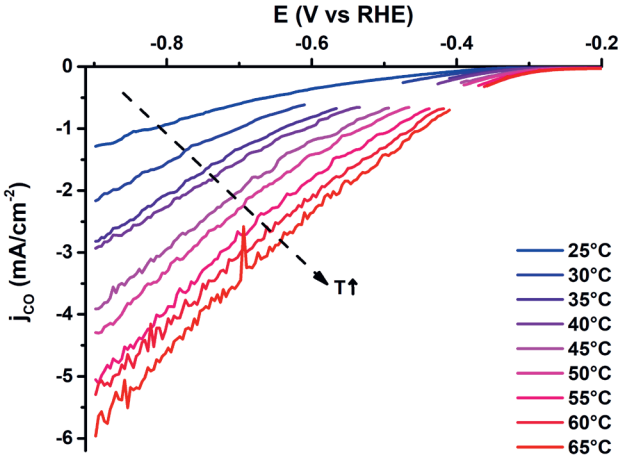

Figure 2.2 The partial current density for CO formation at different temperatures at constant CO_2 concentrations in 0.1M $NaHCO_3$ on a gold RRDE at 2500 rpm and 20 mV/s.

For all the other temperatures, we determined the required partial pressure of CO_2 to obtain this same CO_2 concentration. Figure 2.2 shows the partial current density of CO formation with increasing temperature at the same CO_2 concentration at each temperature. The activity for the CO2RR increases with temperature and the increase in activity is larger in Figure 2.2 than in Figure 2.1a. Based on Figure A.5, this result is to be expected as Figure 2.1 is a convolution of the effect of temperature and the decreasing activity due to lower CO2 concentrations. This also shows that the enhancing effect of temperature on the activity is larger than the suppressing effect of CO_2 concentration, resulting in a net increase in activity in Figure 2.1a. Furthermore, no plateau in activity as a function of temperature is observed in Figure 2.2. This suggests that the plateau observed in Figure 2.1 is related to a decreasing concentration of CO_2 in solution. From 55 ^{0}C onwards, the effect of temperature is not strong enough anymore to compensate for the decrease in activity due to the lower CO_2 concentration.

As the CO_2 concentration is lower at higher temperatures, we need to consider mass transport. Similar to our result, Löwe et al.[41] observed an optimum in the CO2RR selectivity at 50 ^{0}C. They explained this optimum as a compromise between decreasing solubility and the increasing diffusion coefficient. With our RRDE setup, we can control mass transport by varying the rotation rate and we do not observe this optimum in mass transport. Figure 2.3 shows the CO_2 activity at different rotation rates at different temperatures. At 25 ^{0}C, it can be seen that there is no rotation rate dependence up to high overpotentials. This suggests that there are no mass transport limitations at this temperature. At 40 ^{0}C, we see some rotation rate dependence, with higher partial current densities at higher rotation rates. The potential at which this rotation dependence sets in shifts to lower values at 55 ^{0}C; the "critical" current density appears around -1.0 mA/cm^2 for all three temperatures. Below this current, there seems to be no positive effect of faster mass transport at any temperature, so an increase in diffusivity should not lead to an increase in activity. Moreover, when the Levich equation is used to calculate the limiting current densities (Table A.3), we observe that the limiting current densities decrease with temperature (104, 95 and 90 mA/cm^2 respectively for 25 ^{0}C, 40 ^{0}C and 55 ^{0}C at 2500 rpm) but they are still considerably higher than the measured current densities, indicating that the increase in activity is mainly caused by an increase in kinetics and not due to the increasing diffusion coefficient. Furthermore, Koutecky-Levich analysis (Figure A.7, Table A.4) at the different temperatures also shows that the kinetic current increases and the Levich constant decreases with temperature.

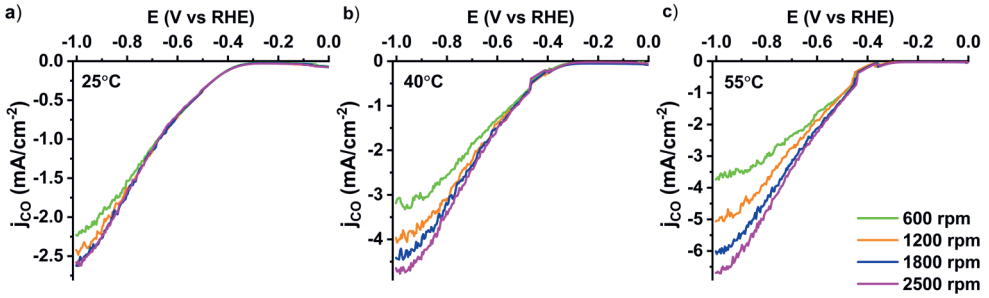

Figure 2.3 Partial current densities for CO formation at different rotation rates at 25 (a) 40 (b) and 55 ^{0}C (c) in 0.1M $NaHCO_3$ at 20 mV/s

Interestingly, even below -1.0 mA/cm^2, where no mass transport limitations are present, we observe the plateau in the CO2RR activity for higher temperatures than 55 ^{0}C. As mentioned, the calculated limiting current densities are much larger than observed in Figure 2.3. This has been observed before and has been attributed to the homogenous reaction 2.8 which consumes CO_2 and lowers its concentration at the surface.[73,76]

$$CO_2 + OH^- \rightarrow HCO_3^- \qquad (2.8)$$

At the higher current densities not only more CO_2 is consumed in the electrochemical reaction but also more OH^- is generated which consumes more CO_2 in the homogenous reaction, increasing the effect of the rotation rate. Moreover, at higher temperatures, the reaction rate of the homogeneous reaction of CO_2 increases, so even at the same local pH, more CO_2 will be consumed due to reaction 3.[77]

Figure 2.1b shows that also hydrogen evolution activity increases with temperature. It can be observed that the activity for the HER does not show a plateau as a function of temperature. Although it has been shown recently that the HER can show an unexpected mass transport dependence,[78] this is not expected to limit the HER at higher temperatures as the near-surface cation concentration is not decreasing with increasing temperatures. As a control experiment, we also studied the effect of temperature on the HER without CO_2 in solution. Figure A.8 shows that also in this case, the HER increases with temperature and no plateau is observed.

Figure 2.4a shows the FE towards CO as a function of both temperature and applied potential. An optimal potential around -0.55 V vs RHE is observed, in agreement with previous experiments.[52] The trend as a function of temperature is

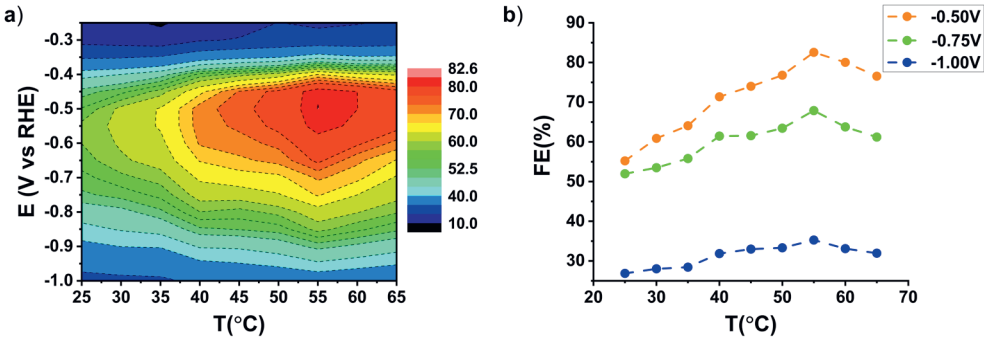

Figure 2.4 Faradaic efficiency for CO formation plotted as (a) a function of both potential and temperature and (b) as a function of temperature at distinct potentials for a gold RRDE at 2500 rpm in 0.1M $NaHCO_3$

less clear and depends on potential. Figure 2.4b shows that at medium overpotentials, the FE towards CO has a maximum at 55 ^{0}C. This optimum is logical as from this temperature onwards the CO2RR activity starts plateauing, while the HER rate keeps increasing with temperature. When the CO_2 concentration is kept constant, as in Figure 2.2, the FE does not decrease at these temperatures but plateaus. At higher overpotentials, the optimum remains at 55 ^{0}C, however the differences in FE between different temperatures become smaller.

Up to now, we have looked at the effect of temperature on CO_2 reduction mostly in a qualitative way. To have a more quantitative evaluation, we define ratios of partial current densities according to equation 2.9:

$$r_T = \frac{j_T}{j_{25°C}} \qquad (2.9)$$

where *r* is the ratio, and *j* is the partial current density. Table A.5 plots these ratios as a function of temperature and applied potential. Not surprisingly, these ratios increase with temperature. However, it can also be observed that with increasing overpotential, the effect of temperature becomes smaller. Whereas at -0.4 V the activity at 55 ^{0}C is almost 4 times higher than at 25 ^{0}C, the ratio has decreased to a factor 2 at -1.0V. This explains why the effect of temperature on the FE decreases at more negative potentials. In most studies for CO_2 reduction, these higher overpotentials are used and it is thus important to realize that the effect of temperature will be smaller (though still significant) at these potentials. We will go into more detail later why it is to be expected from theory that the temperature effect depends on potential.

2.3.2 Activation energies

From the temperature dependent experiments we can obtain the apparent activation energy for the CO_2 reduction on gold using the Arrhenius equation:

$$k = Ae^{\frac{-E_a}{RT}} \qquad (2.10)$$

where k is the reaction rate constant, A is the pre-exponential factor, E_a is the activation energy, R is the gas constant and T the absolute temperature. Since the exchange current density depends on the reaction rate constant, the j_0 will also follow an Arrhenius relation and equation 2.11a can be used. In order to obtain the "real" activation energy, we need to correct for the T-dependence of the CO2 concentration and equation 2.11b is derived from equation 2.11a (see SI).

$$\ln(j_0) = \ln(A') - \frac{E_a}{R} * \frac{1}{T} \qquad (2.11a)$$

$$\ln(j_0) + \ln\left(\frac{C_{25^\circ C}}{C_T}\right) = \ln(A') - \frac{E_a}{R} * \frac{1}{T} \qquad (2.11b)$$

where j_0 is the exchange current density, A' the pre-exponential factor, E_a the activation energy, R the gas constant, T the absolute temperature, $C_{25^\circ C}$ and C_T the concentration of CO_2, at 25 ^{0}C and a given temperature, respectively.

Figure 2.5 shows the corrected Arrhenius plot for CO_2 reduction in 0.1M $NaHCO_3$ on gold using the standard exchange current densities. From the slope of the Arrhenius plot, the apparent activation energy is determined to be 61 ±2 kJ/mol, according to equation 2.11b. This value applies (as extrapolated to) to the standard equilibrium potential; values for the activation energy at different overpotentials will be discussed below. As mentioned in the experimental section, the standard potential of the CO2RR also changes with temperature and in the above calculations this has been taken into account. If we would calculate all exchange current densities at -0.1 V, the standard potential at 25 ^{0}C, there is only about 1 kJ/mol difference.

The corrected apparent activation energy takes the variable CO_2 concentration into account and is close to the apparent activation energy determined from the activities at constant CO_2 concentration of Figure 2.2, supporting our correction method. With constant CO_2 concentration the apparent activation energy is 60 kJ/mol (Figure A.10). Moreover, our apparent activation energy is comparable to barriers calculated with DFT in the literature [79] (though such comparisons have certain pitfalls regarding the exact assumptions made in the computations).

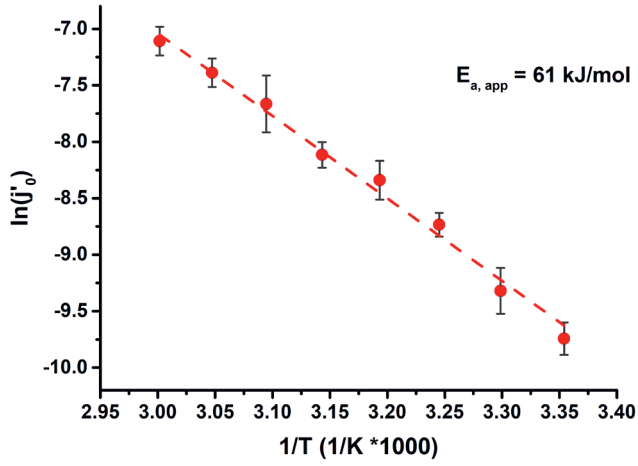

Figure 2.5 Arrhenius plot of CO_2 standard reduction current in 0.1M NaHCO3 in the temperature range of 25-60 ^{0}C

The apparent activation energy of the HER is expected to be lower than for the CO2RR as the activity of the HER is less temperature dependent than that of the CO2RR. For an accurate independent measurement of the activation energy for HER, we have performed experiments without CO_2 in solution, from which we determined the apparent activation energy for the HER to be 25 ± 3 kJ/mol (Figure A.11). In the literature, the apparent activation energy for the HER on Pt has been reported to be between 9.5 and 18 kJ/mol, depending on the facet,[79] although other studies found considerable higher activation energies.[80] On Ag an activation energy between 20 and 30 kJ/mol has been found.[81,82] Thus, it seems that the activation energy of the HER is indeed lower than that for the CO2RR, explaining the larger increase in activity with temperature for the latter.

The activation energy is expected to be dependent on the potential. This is an underlying assumption of the Butler-Volmer equation (equation 2.12[83]), describing the relationship between the applied potential and Faradaic current. Equations 2.13a and b[84] are used to derive the Butler-Volmer equation from the Arrhenius equation, linking activation energy to potential.

$$j = j_0 \left\{ exp\left[\frac{\alpha_c F\eta}{RT}\right] - exp\left[-\frac{\alpha_a F\eta}{RT}\right]\right\} \qquad (2.12)$$

$$\Delta G_c^{\ddagger} = \Delta G_{0c}^{\ddagger} + a_c F\eta \qquad (2.13a)$$

$$\Delta G_a^{\ddagger} = \Delta G_{0a}^{\ddagger} + a_a F\eta \qquad (2.13b)$$

$$\Delta H_c^{\ddagger} = \Delta H_{0c}^{\ddagger} + \alpha_{c,H} F\eta \qquad (2.13c)$$

where $\Delta G_{Oc}^{\ddagger}$ is the free energy of activation at the standard equilibrium potential, $\Delta H_{Oc}^{\ddagger}$ the enthalpy of activation at the standard equilibrium potential, α_c and α_a the cathodic and anodic transfer coefficient respectively, j_0 the standard exchange current density and η the overpotential.

Equation 2.13c is similar to equation 2.13a, but is used instead because the activation enthalpy is more directly related to the apparent activation energy determined using the Arrhenius equation.[85] Both equations state that the activation energy depends linearly on the applied potential.[86,87] At zero overpotential, the same apparent activation energy is obtained as determined from the standard exchange current density. Figure 2.6 and A.12 show the experimental relation between activation enthalpy and potential, which is indeed linear. The apparent activation enthalpy at zero overpotential in $NaHCO_3$ is 59 ± 4 kJ/mol, which is similar to the 61 kJ/mol determined with the exchange current densities. Moreover, from the slope we can determine the enthalpic transfer coefficient α_H to be 0.3, independent of cation identity and concentration (Figure A.12/13). Commonly the Butler-Volmer transfer coefficient α_c is assumed to be 0.5 as the first electron transfer is considered the rate limiting step for CO_2 reduction on gold,[75,88–90]

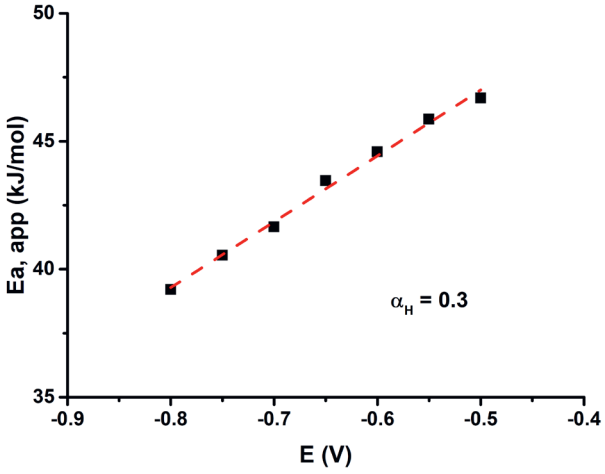

Figure 2.6 The apparent activation energy of CO_2 reduction towards CO in 0.1M $NaHCO_3$ plotted against the applied potential

although there is still some debate around this.[70,91] Conway et al. have discussed in detail this difference between the enthalpic part of the transfer coefficient and the Butler-Volmer transfer coefficient:[86,87,92–94]

$$\alpha_c = \alpha_H + T\alpha_s \qquad (2.14)$$

The entropic part of the transfer coefficient can be obtained by plotting the natural logarithm of the pre-exponential factor against the potential[87] (Figure A.14) and from the slope, α_s has been calculated to be 5 * 10^{-4} K^{-1} for CO_2 reduction on gold. At room temperature, this is roughly 0.15 meaning that the enthalpic part dominates the transfer coefficient. This implies that in this catalytic process most of the potential dependence of the rate is due to changes in the height of the potential energy barrier, but the entropy of activation is not negligible. This is in contrast to a process such as oxygen reduction, where the opposite has been found.[92,95]

2.3.3 Cation effect

It is well known that cations affect the CO_2 reduction rate,[11–14] but this effect has not yet been studied in combination with the temperature effect. Figure 2.7 shows that there is an increase in activity in the order Li^+ < Na^+ < K^+ < Cs^+. This order is observed at both 25 ^{0}C and 50 ^{0}C. The apparent activation energy decreases gradually from 65 ±2 kJ/mol (Li^+) to 54 ±2 kJ/mol (Cs^+) (see Table 2.1). A lower activation energy results in a weaker temperature effect, therefore the differences in activity are expected to become smaller with increasing temperature. This effect is difficult to observe in Figure 2.7 as the temperature

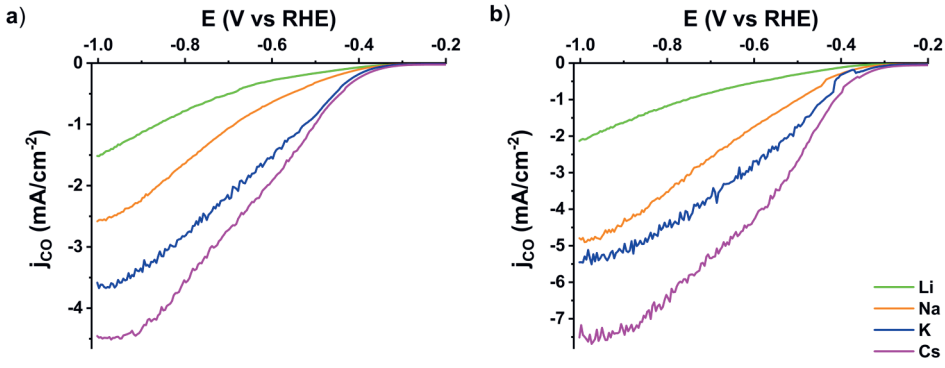

Figure 2.7 The partial current densities for the CO2RR for different cations at 25^{0}C (a) and 50^{0}C (b) on a gold RRDE at 2500 rpm at 20 mV/s

interval seems to be too small to observe major differences. For the pre- exponential factor a comparable (albeit reversed) tendency is observed, with Cs^+ having the lowest value. If extrapolated to high temperatures, the cation effect would reverse and Cs^+ would become the least active, but most likely these trends cannot be extrapolated in this way.

Similar trends can be observed if the concentration of cations is increased by adding $NaClO_4$ to 0.1M $NaHCO_3$ as seen in Table 2.2. The apparent activation energy decreases from 61 ±2 kJ/mol in 0.1M Na^+ to 51 ±3 kJ/mol in 0.5M Na^+ and the pre-exponential factor decreases in the same sequence. The decreasing activation energy going from Li^+ to Cs^+ agrees with all of the most proposed mechanisms for the cation effect and can therefore not be used to differentiate between them. The theory which states that the local potential in the outer Helmholtz layer changes with cation predicts this decrease in activation energy. Furthermore, the explanation of stabilizing intermediates due to the electric field, or as recently proposed by a short-range electrostatic interaction,[48] would also lead to lower activation energies for Cs^+ compared to Li^+. According to the buffering theory, cations influence the local pH and consequently the local CO_2 concentration differently as Cs^+ is a better buffer than Li^+.[13] This leads to differences in coverage and thus a difference in apparent activation energy. However, it is unlikely that the cation buffering is the cause of the cation effect observed in this study as we have efficient mass transport and the cation effect is already observed at very low current densities. Most likely the decrease in activation energy is either due the change in local potential or to the stabilization of intermediates by to the cations.

A smaller pre-exponential factor going from Li^+ to Cs^+ is likely a limitation of the extrapolation of the data to infinite temperature. This so-called compensation effect has been observed in literature before and arises because the pre-exponential factor and the activation energy are determined from the same Arrhenius plot.[80] However, this observation could in principle also fit in the picture where the concentration of Cs^+ near the surface is higher than that of Li^+. This might make it more difficult for the CO_2 to reach the surface if the concentration is high. It has been shown that the concentration of cations can be considerably higher at the interface than the bulk concentration: a recent computational study has suggested that the concentration of cations at the surface could reach up to 1.5 M with a bulk concentration of only 0.1 M.[96] 1.5 M of K^+ would fill up to 34 percent of the space (see calculation in the SI), making it reasonable to argue this could hinder the CO_2 to reach the surface. This hindrance would decrease the pre-exponential factor as this can be seen as the likelihood of the reactant reaching the electrode surface.[97] This likelihood would decrease if more cations screened the surface. This interpretation is supported by the rapid decrease of the pre-exponential factor with

increasing cation concentration. Although this is certainly an oversimplification of the interpretation of the pre-exponential factor, it could carry an element of truth and helps visualizing how cations can influence this parameter. Nevertheless, for the time being, we interpret the observations as a compensation effect, the nature of which is still very much debated.[98]

Table 2.1 Apparent activation energies both uncorrected and corrected, and the pre-exponential factor for the CO2RR in different 0.1M bicarbonate electrolytes

	$E_{a,app}$ (kJ/mol)	$E_{a,app}^{corrected}$ (kJ/mol)	ln(A) (A in cm/s)
Li^+	48	65	7.1
Na^+	44	61	6.8
K^+	39	57	6.1
Cs^+	36	54	5.7

Table 2.2 Apparent activation energies both uncorrected and corrected, and the pre-exponential factor for the CO2RR in NaHCO3 electrolytes with different concentrations of Na

	$E_{a,app}$ (kJ/mol)	$E_{a,app}^{corrected}$ (kJ/mol)	ln(A) (A in cm/s)
0.1 M	44	61	6.8
0.2 M	39	56	5.4
0.3 M	36	53	4.0
0.5 M	33	51	3.0

2.4 Conclusion

In this paper we have shown that both the activity and selectivity of electrochemical CO_2 reduction can benefit from elevating the temperature of the electrochemical system. However, there is a complex balance between the increase in kinetics and the decreasing solubility of CO_2. This balance results in a limiting temperature of 55 ^{0}C, after which the CO2RR activity plateaus and the selectivity decreases. Moreover, because of the limiting amount of CO_2 in solution, mass transfer becomes more important at higher temperatures, though we emphasize that at all temperatures the system is still rather far from the theoretical mass transport limited CO_2 reduction current. If the CO_2 solubility can be increased, for

example by increasing the pressure of CO_2, it is to be expected that the optimum temperature for CO_2 reduction can be further increased. The effect of temperature is largest at lower overpotentials and decreases with increasing overpotential as the activation energy is influenced by the potential. The apparent activation energy for the CO2RR is 61 kJ/mol in 0.1M $NaHCO_3$. This activation energy depends on the electrolyte and decreases both with cation concentration and identity. This is in agreement with the cation effect known in literature and shows that this effect becomes less significant at elevated temperatures. Moreover, we show that the enthalpic part of the transfer coefficient for the CO2RR on gold is 0.3. This indicates that the enthalpy plays a dominant role in this process, although the entropy contribution cannot be neglected. This study has focused on Au as a model catalyst for CO_2 reduction as it provides a simple system with only CO as the product of the CO2RR. This relative simplicity made it possible to study the basic effects of temperature. Future work will study this effect on other catalysts such as Cu and investigate how the product distribution of the CO2RR changes with temperature. Furthermore, pressurized experiments should be performed to broaden the temperature range that can be studied.

References

1. Nitopi, S. *et al. Chemical Reviews* vol. 119 7610–7672 Preprint at (2019).
2. Birdja, Y. Y. *et al. Nat Energy* **4**, 732–745 (2019).
3. Varela, A. S. *Curr Opin Green Sustain Chem* **26**, 100371 (2020).
4. Narayanaru, S., Chinnaiah, J., Phani, K. L. & Scholz, F. *Electrochim Acta* **264**, 269–274 (2018).
5. Liu, X. *et al. Nat Commun* **10**, 32 (2019).
6. Jiang, X., Li, H., Yang, Y. & Gao, D. *J Mater Sci* **55**, 13916–13926 (2020).
7. Schouten, K. J. P., Pérez Gallent, E. & Koper, M. T. M. *Journal of Electroanalytical Chemistry* **716**, 53–57 (2014).
8. Varela, A. S., Kroschel, M., Reier, T. & Strasser, P. *Catal Today* **260**, 8–13 (2016).
9. Kas, R., Kortlever, R., Yılmaz, H., Koper, M. T. M. & Mul, G. *ChemElectroChem* **2**, 354–358 (2015).
10. Singh, M. R., Clark, E. L. & Bell, A. T. *Physical Chemistry Chemical Physics* **17**, 18924–18936 (2015).
11. Murata, A. & Hori, Y. *Bulletin of the Chemical Society of Japan* vol. 64 123–127 (1991).
12. Resasco, J. *et al. J Am Chem Soc* **139**, 11277–11287 (2017).
13. Singh, M. R., Kwon, Y., Lum, Y., Ager, J. W. & Bell, A. T. *J Am Chem Soc* **138**, 13006–13012 (2016).
14. Ringe, S. *et al. Energy Environ Sci* 17–25 (2019) doi:10.1039/c9ee01341e.
15. Resasco, J., Lum, Y., Clark, E., Zeledon, J. Z. & Bell, A. T. *ChemElectroChem* **5**, 1064–1072 (2018).
16. Huang, Y., Ong, C. W. & Yeo, B. S. *ChemSusChem* **11**, 3299–3306 (2018).
17. Schouten, K. J. P., Qin, Z., Gallent, E. P. & Koper, M. T. M. *J Am Chem Soc* **134**, 9864–9867 (2012).
18. Schouten, K. J. P., Pérez Gallent, E. & Koper, M. T. M. *ACS Catal* **3**, 1292–1295 (2013).
19. Pérez-Gallent, E., Marcandalli, G., Figueiredo, M. C., Calle-Vallejo, F. & Koper, M. T. M. *J Am Chem Soc* **139**, 16412–16419 (2017).
20. Todoroki, N. *et al. ACS Catal* **9**, 1383–1388 (2019).
21. Jia, Y., Jiang, K., Wang, H. & Yao, X. *Chem* **5**, 1371–1397 (2019).
22. Mariano, R. G., McKelvey, K., White, H. S. & Kanan, M. W. *Science* **358**, 1187–1192 (2017).
23. Vickers, J. W., Alfonso, D. & Kauffman, D. R. *Energy Technology* **5**, 775–795 (2017).
24. Chen, C., Zhang, B., Zhong, J. & Cheng, Z. *J Mater Chem A Mater* **5**, 21955–21964 (2017).
25. da Silva, A. H. M. *et al. Journal of Electroanalytical Chemistry* **880**, (2021).
26. Jiang, K. *et al. ACS Energy Lett* **5**, 1206–1214 (2020).
27. Lum, Y., Yue, B., Lobaccaro, P., Bell, A. T. & Ager, J. W. *Journal of Physical Chemistry C* **121**, 14191–14203 (2017).
28. Scheepers, F. *et al. Appl Energy* **283**, 1–11 (2021).
29. Chandrasekar, A., Flynn, D. & Syron, E. *Int J Hydrogen Energy* (2021)

30. Carmo, M., Fritz, D. L., Mergel, J. & Stolten, D. *Int J Hydrogen Energy* **38**, 4901–4934 (2013).
31. Babic, U., Suermann, M., Büchi, F. N., Gubler, L. & Schmidt, T. J. *J Electrochem Soc* **164**, F387–F399 (2017).
32. Dufek, E. J., Lister, T. E. & McIlwain, M. E. *J Appl Electrochem* **41**, 623–631 (2011).
33. Pino, F. J., Valverde, L. & Rosa, F. *J Power Sources* **196**, 4418–4426 (2011).
34. Lee, W., Kim, Y. E., Youn, M. H., Jeong, S. K. & Park, K. T. *Angewandte Chemie - International Edition* **57**, 6883–6887 (2018).
35. Kim, H. Y. *et al. Int J Hydrogen Energy* **39**, 16506–16512 (2014).
36. Han, L., Zhou, W. & Xiang, C. *ACS Energy Lett* **3**, 855–860 (2018).
37. Gabardo, C. M. *et al. Joule* **3**, 2777–2791 (2019).
38. Endrődi, B. *et al. Prog Energy Combust Sci* **62**, 133–154 (2017).
39. Ahn, S. T., Abu-baker, I. & Palmore, G. T. R. *Catal Today* **288**, 24–29 (2017).
40. Hori, Y., Kikuchi, K., Murata, A. & Suzuki, S. *Chem Lett* **15**, 897–898 (1986).
41. Löwe, A. *et al. ChemElectroChem* **6**, 4497–4506 (2019).
42. Thorson, M. R., Siil, K. I. & Kenis, P. J. A. *J Electrochem Soc* **160**, F69–F74 (2012).
43. Kim, H., Park, H. S., Hwang, Y. J. & Min, B. K. *The Journal of Physical Chemistry C* **121**, 22637–22643 (2017).
44. Malkani, A. S., Anibal, J. & Xu, B. *ACS Catal* **10**, 14871–14876 (2020).
45. Waegele, M. M., Gunathunge, C. M., Li, J. & Li, X. *Journal of Chemical Physics* **151**, 1DUMMT (2019).
46. Zhang, F. & Co, A. C. *Angewandte Chemie - International Edition* **59**, 1674–1681 (2020).
47. Ayemoba, O. & Cuesta, A. *ACS Appl Mater Interfaces* **9**, 27377–27382 (2017).
48. Monteiro, M. C. O. *et al. Nat Catal* **4**, (2021).
49. Kauffman, D. R. *et al. ACS Appl Mater Interfaces* **7**, 15626–15632 (2015).
50. Kim, D., Resasco, J., Yu, Y., Asiri, A. M. & Yang, P. *Nat Commun* **5**, 4948 (2014).
51. Cave, E. R. *et al. Physical Chemistry Chemical Physics* **19**, 15856–15863 (2017).
52. Goyal, A., Marcandalli, G., Mints, V. A. & Koper, M. T. M. *J Am Chem Soc* **142**, 4154–4161 (2020).
53. Marcandalli, G., Goyal, A. & Koper, M. T. M. *ACS Catal* 4936–4945 (2021)
54. Vos, J. G. & Koper, M. T. M. *Journal of Electroanalytical Chemistry* **850**, 113363 (2019).
55. Łukaszewski, M., Soszko, M. & Czerwiński, A. *Int. J. Electrochem. Sci* **11**, 4442–4469 (2016).
56. Wildgoose, G. G., Giovanelli, D., Lawrence, N. S. & Compton, R. G. *Electroanalysis* 16 421–433 (2004).
57. Greeley, R. S., Smith Jr, W. T., Stoughton, R. W. & Lietzke, M. H. *J Phys Chem* **64**, 652–657 (1960).
58. Macdonald, D. D., Scott, A. C. & Wentrcek, P. *J Electrochem Soc* **126**, 908–911 (1979).
59. Öijerholm, J., Forsberg, S., Hermansson, H.-P. & Ullberg, M. *J Electrochem Soc* **156**, P56 (2009).
60. Harned, H. S. & Davis Jr, R. *J Am Chem Soc* **65**, 2030–2037 (1943).
61. Duan, Z. & Sun, R. *Chem Geol* **193**, 257–271 (2003).

62. Plummer, L. N. & Busenberg, E. *Geochim Cosmochim Acta* **46**, 1011–1040 (1982).
63. Lu, W., Guo, H., Chou, I. M., Burruss, R. C. & Li, L. *Geochim Cosmochim Acta* **115**, 183–204 (2013).
64. Tamimi, A., Rinker, E. B. & Sandall, O. C. *J Chem Eng Data* **39**, 330–332 (1994).
65. Unver, A. A. & Himmelblau, D. M. *J Chem Eng Data* **9**, 428–431 (1964).
66. Gründler, P., Kirbs, A. & Dunsch, L. *ChemPhysChem* **10**, 1722–1746 (2009).
67. Lobaccaro, P. *et al. Physical Chemistry Chemical Physics* **18**, 26777–26785 (2016).
68. Monteiro, M. C. O., Liu, X., Hagedoorn, B. J. L., Snabilié, D. D. & Koper, M. T. M. *ChemElectroChem* 1–8 (2021).
69. Hall, A. S., Yoon, Y., Wuttig, A. & Surendranath, Y. *J Am Chem Soc* **137**, 14834–14837 (2015).
70. Ringe, S. *et al. Nat Commun* **11**, (2020).
71. Noda, H., Ikeda, S., Yamamoto, A., Einaga, H. & Ito, K. *Bull Chem Soc Jpn* **68**, 1889–1895 (1995).
72. Kyriacou, G. Z. & Anagnostopoulos, A. K. *J Appl Electrochem* **23**, 483–486 (1993).
73. Marcandalli, G., Villalba, M. & Koper, M. T. M. (2021)
74. Dunwell, M. *et al. J Am Chem Soc* **139**, 3774–3783 (2017).
75. Wuttig, A., Yaguchi, M., Motobayashi, K., Osawa, M. & Surendranath, Y. *Proc Natl Acad Sci U S A* **113**, E4585–E4593 (2016).
76. Rebouillat, S., Lyons, M. E. G. & Bannon, T. *Journal of Solid State Electrochemistry* **3**, 215–230 (1999).
77. Schulz, K. G., Riebesell, U., Rost, B., Thoms, S. & Zeebe, R. E. *Mar Chem* **100**, 53–65 (2006).
78. Goyal, A. & Koper, M. T. M. *Angewandte Chemie - International Edition* **60**, 13452–13462 (2021).
79. Liu, M. *et al. Nature* **537**, 382–386 (2016).
80. Marković, N. M., Grgur, B. N. & Ross, P. N. *Journal of Physical Chemistry B* **101**, 5405–5413 (1997).
81. He, Z. Da, Wei, J., Chen, Y. X., Santos, E. & Schmickler, W. *Electrochim Acta* **255**, 391–395 (2017).
82. Eberhardt, D., Santos, E. & Schmickler, W. *Journal of Electroanalytical Chemistry* **461**, 76–79 (1999).
83. Kang, J., Lin, C. H., Yao, Y. & Chen, Y. X. *Chinese Journal of Chemical Physics* **27**, 63–68 (2014).
84. Bockris, J. O. & Nagy, Z. *J. Chern. Ed.* **50**, 839–843 (1973).
85. Protsenko, V. S. & Danilov, F. I. *Journal of Electroanalytical Chemistry* **651**, 105–110 (2011).
86. Berry, R. S., Rice, S. A. & Ross, J. (Oxford University Press, 2000).
87. Conway, B. E. & Wilkinson, D. P. *Electrochim Acta* **38**, 997–1013 (1993).
88. Gojković, S. L., Zečević, S. K. & Dražić, D. M. *Journal of Electroanalytical Chemistry* **399**, 127–133 (1995).
89. Wuttig, A., Yoon, Y., Ryu, J. & Surendranath, Y. *J Am Chem Soc* **139**, 17109–17113 (2017).

90. Zhang, B. A., Ozel, T., Elias, J. S., Costentin, C. & Nocera, D. G. *ACS Cent Sci* **5**, 1097–1105 (2019).
91. Dunwell, M., Luc, W., Yan, Y., Jiao, F. & Xu, B. *ACS Catal* **8**, 8121–8129 (2018).
92. Solorza-Feria, O. & Durón, S. *Int J Hydrogen Energy* **27**, 451–455 (2002).
93. Conway, B. E. & Wilkinson, D. F. *Journal of Electroanalytical Chemistry* **214**, 633–653 (1986).
94. Conway, B. E., Tessier, D. F. & Wilkinson, D. P. *Journal of Electroanalytical Chemistry* **199**, 249–269 (1986).
95. Clouser, S. J., Huang, J. C. & Yeager, E. *J Appl Electrochem* **23**, 597–605 (1993).
96. Weitzner, S. E. *et al. Journal of Physical Chemistry Letters* **11**, 4113–4118 (2020).
97. Costentin, C., Louault, C., Robert, M., Rogé, V. & Savéant, J. M. *Physical Chemistry Chemical Physics* **14**, 1581–1584 (2012).
98. Bligaard, T. *et al. J Phys Chem B* **107**, 9325–9331 (2003).